

# Search for the Proton Decay Mode $p \rightarrow \bar{\nu}K^+$ with KamLAND

K. Asakura,<sup>1</sup> A. Gando,<sup>1</sup> Y. Gando,<sup>1</sup> T. Hachiya,<sup>1</sup> S. Hayashida,<sup>1</sup> H. Ikeda,<sup>1</sup> K. Inoue,<sup>1,2</sup> K. Ishidoshiro,<sup>1</sup> T. Ishikawa,<sup>1</sup> S. Ishio,<sup>1</sup> M. Koga,<sup>1,2</sup> R. Matsuda,<sup>1</sup> S. Matsuda,<sup>1</sup> T. Mitsui,<sup>1</sup> D. Motoki,<sup>1</sup> K. Nakamura,<sup>1,2</sup> S. Obara,<sup>1</sup> Y. Oki,<sup>1</sup> T. Oura,<sup>1</sup> I. Shimizu,<sup>1</sup> Y. Shirahata,<sup>1</sup> J. Shirai,<sup>1</sup> A. Suzuki,<sup>1</sup> H. Tachibana,<sup>1</sup> K. Tamae,<sup>1</sup> K. Ueshima,<sup>1</sup> H. Watanabe,<sup>1</sup> B.D. Xu,<sup>1</sup> Y. Yamauchi,<sup>1</sup> H. Yoshida,<sup>1,\*</sup> A. Kozlov,<sup>2</sup> Y. Takemoto,<sup>2</sup> S. Yoshida,<sup>3</sup> K. Fushimi,<sup>4</sup> C. Grant,<sup>5,†</sup> A. Piepke,<sup>5,2</sup> T.I. Banks,<sup>6</sup> B.E. Berger,<sup>6,2</sup> S.J. Freedman,<sup>6,‡</sup> B.K. Fujikawa,<sup>6,2</sup> T. O'Donnell,<sup>6</sup> J.G. Learned,<sup>7</sup> J. Maricic,<sup>7</sup> M. Sakai,<sup>7</sup> S. Dazeley,<sup>8,§</sup> R. Svoboda,<sup>8,†</sup> L.A. Winslow,<sup>9</sup> Y. Efremenko,<sup>10,2</sup> H.J. Karwowski,<sup>11</sup> D.M. Markoff,<sup>11</sup> W. Tornow,<sup>11,2</sup> J.A. Detwiler,<sup>12</sup> S. Enomoto,<sup>12,2</sup> and M.P. Decowski<sup>13,2</sup>

(The KamLAND Collaboration)

<sup>1</sup>Research Center for Neutrino Science, Tohoku University, Sendai, Miyagi 980-8578, Japan

<sup>2</sup>Kavli Institute for the Physics and Mathematics of the Universe (WPI), University of Tokyo, Kashiwa, Chiba 277-8583, Japan

<sup>3</sup>Graduate School of Science, Osaka University, Toyonaka, Osaka 560-0043, Japan

<sup>4</sup>Faculty of Integrated Arts and Science, University of Tokushima, Tokushima, 770-8502, Japan

<sup>5</sup>Department of Physics and Astronomy, University of Alabama, Tuscaloosa, Alabama 35487, USA

<sup>6</sup>Physics Department, University of California, Berkeley, and

Lawrence Berkeley National Laboratory, Berkeley, California 94720, USA

<sup>7</sup>Department of Physics and Astronomy, University of Hawaii at Manoa, Honolulu, Hawaii 96822, USA

<sup>8</sup>Department of Physics and Astronomy, Louisiana State University, Baton Rouge, Louisiana 70803, USA

<sup>9</sup>Massachusetts Institute of Technology, Cambridge, Massachusetts 02139, USA

<sup>10</sup>Department of Physics and Astronomy, University of Tennessee, Knoxville, Tennessee 37996, USA

<sup>11</sup>Triangle Universities Nuclear Laboratory, Durham, North Carolina 27708, USA and

Departments of Physics at Duke University, North Carolina Central University, and the University of North Carolina at Chapel Hill

<sup>12</sup>Center for Experimental Nuclear Physics and Astrophysics, University of Washington, Seattle, Washington 98195, USA

<sup>13</sup>Nikhef and the University of Amsterdam, Science Park, Amsterdam, the Netherlands

(Dated: November 20, 2018)

We present a search for the proton decay mode  $p \rightarrow \bar{\nu}K^+$  based on an exposure of 8.97 kton-years in the KamLAND experiment. The liquid scintillator detector is sensitive to successive signals from  $p \rightarrow \bar{\nu}K^+$  with unique kinematics, which allow us to achieve higher detection efficiency than previous searches in water Cherenkov detectors. We find no evidence of proton decays for this mode. The expected background comes mainly from atmospheric neutrinos, the total background is  $0.9 \pm 0.2$  events. The non-background subtracted limit on the partial proton lifetime is  $\tau/B(p \rightarrow \bar{\nu}K^+) > 5.4 \times 10^{32}$  years at 90% C.L.

PACS numbers: 12.10.Dm, 13.30.-a, 12.60.Jv, 11.30.Fs, 29.40.Mc

## I. INTRODUCTION

Extensions of the Standard Model (SM) of particle physics, such as supersymmetric grand unified theories (SUSY-GUTs) [1, 2] predict that the three SM coupling constants are unified at a scale of  $\sim 2 \times 10^{16}$  GeV. Proton decay is an indispensable probe to determine the unified scale experimentally. In SUSY-GUT models, the proton decay mode  $p \rightarrow \bar{\nu}K^+$  is expected to be the leading process through the color-triplet Higgs exchange in dimension-five operator interactions [3]. At the same time, the predicted decay rate of  $p \rightarrow e^+\pi^0$  can be highly suppressed by masses, and is consistent with the current experimental lower limits on the partial lifetime [4–6].

This paper reports on an experimental search for the proton decay mode  $p \rightarrow \bar{\nu}K^+$  with KamLAND, a 1 kton liquid scintillator (LS) detector [7], for the first time. Previous sensitive searches were performed by the Super-Kamiokande collaboration with a fiducial mass of 22.5 kton [8–10]. In water Cherenkov detectors, the direct signal from the decay of  $K^+$  is not visible because its momentum is below the Cherenkov threshold. The Super-Kamiokande experiment made it possible to search this decay mode based on the coincidence detection of prompt Cherenkov signals from the remaining nucleus de-excitation  $\gamma$ -ray and delayed  $K^+$  decay daughters, or kinematical selections of  $K^+$  decay daughters, reporting the most stringent limit of  $\tau/B(p \rightarrow \bar{\nu}K^+) > 5.9 \times 10^{33}$  years (90% C.L.) with a 260 kton-year exposure [10]. However, the detection efficiency is low due to backgrounds around the de-excitation  $\gamma$  energy or the limited resolution for reconstructed pion momentum. LS detectors are expected to achieve higher detection efficiency for the decay mode  $p \rightarrow \bar{\nu}K^+$  because they observe scintillation signals from both  $K^+$  and the decay daughters. In addition, the kinetic energy distribution of the decay  $K^+$  measured by scintillation will peak at  $\sim 105$  MeV with a spread caused by nuclear effects and detector resolution, and will provide strong evidence to claim the  $p \rightarrow \bar{\nu}K^+$

\*Present address: Department of Physics, Osaka University, Toyonaka, Osaka 560-0043, Japan

†Present address: Physics Department, University of California, Davis, Davis, California 95616, USA

‡Deceased.

§Present address: Lawrence Livermore National Laboratory, Livermore, California 94550, USA

detection. However, since the time difference between the prompt  $K^+$  and the delayed decay daughters is as short as the time scale of the scintillation response, the two signals need to be effectively separated by the fit to the waveform. That is the greatest challenge in this study. The signal efficiency and background studies presented in this paper are also important for future large LS detectors.

## II. KAMLAND DETECTOR

KamLAND is situated 1 km (2700 m water equivalent) underground in the Kamioka mine in Japan. The detector consists of an 18 m diameter stainless steel spherical shell which defines the boundary between the inner and outer detectors (ID and OD respectively). The inner surface is instrumented with 1325 fast timing 17-inch and 554 20-inch Hamamatsu PMTs facing inwards to a 13 m diameter volume of LS. The density of the LS (80% dodecane, 20% pseudocumene and 1.36 g/liter PPO) is  $0.780 \text{ g/cm}^3$  at  $11.5^\circ\text{C}$ . The LS is contained in a  $135\text{-}\mu\text{m}$ -thick transparent nylon/EVOH (ethylene vinyl alcohol copolymer) balloon, which is mechanically supported by Kevlar ropes and a buffer region of dodecane and isoparaffin oils. The buffer region shields the target from radioactive decays emanating from the walls of the detector and the PMTs. The stainless steel vessel is contained inside the OD, a cylindrical region of pure water instrumented with 225 20-inch PMTs. The OD tags cosmic-ray muons entering the detector and also absorbs neutrons from the surrounding rock.

The 1325 17-inch PMTs alone give a photo-cathode coverage of 22%. The total PMT photo-cathode coverage of the inner detector is 34%. Only the fast timing 17-inch PMTs were used in this analysis. When a PMT channel registers a ‘‘hit’’, the charge as a function of time is recorded by an Analog Transient Waveform Digitizer (ATWD) chip. The KamLAND ATWDs each capture a 128 sample waveform (about 200 ns). Each channel has two sets of three ATWDs, which record waveforms at three available gain levels, providing enough dynamic range to record signals between one and thousands of photo-electrons. The readout time of ATWDs with recorded waveforms is  $30 \mu\text{s}$ , dead time is minimized however, by the dual ( $2 \times 3$  ATWD) system.

The data reported here are based on a total livetime of 9.82 years, collected between January 10, 2003 and May 1, 2014. The data-set is divided into two period: Period-I (3.79 year livetime) refers to data taken up to May 2007, at which time we embarked on a LS purification campaign that continued into 2009. Period-II (6.02 year livetime) refers to data taken during and after the LS purification campaign. We found the scintillation and optical parameters are different between the two periods, so we analyzed the data for each period separately, and finally the results are combined to estimate the partial proton lifetime. We use an LS target mass of 913 ton for the  $p \rightarrow \bar{\nu}K^+$  search, resulting in a total exposure of 8.97 kton-years. Since September 2011, the KamLAND-Zen experiment was launched for the neutrinoless double beta-decay search using a newly introduced  $\beta\beta$  source, 13 tons of Xe-loaded LS in a 3.08-m-diameter inner balloon at the center

of the detector [11]. The volume fraction of Xe-LS to whole LS is 0.014 and the concentration of enriched xenon gas in Xe-LS is less than 3 wt%, so impacts on the proton decay analysis are negligible.

## III. SIMULATION

Simulations were performed in order to understand the event characteristics from  $p \rightarrow \bar{\nu}K^+$  signals and backgrounds in KamLAND. We use Monte Carlo (MC) simulation tools, an event generator for high energy event studies and a general particle tracker applied for the KamLAND detector. In the  $p \rightarrow \bar{\nu}K^+$  search, the remaining background after the cosmic-ray muon rejection is dominated by atmospheric neutrinos. The atmospheric neutrino backgrounds need to be sufficiently removed by requiring the delayed coincidence cuts based on the scintillation signals from the prompt  $K^+$  and the delayed decay daughters, while keeping a certain level of the detection efficiency. The optimum selection was studied by comparing the event characteristics of MC samples from  $p \rightarrow \bar{\nu}K^+$  decays and atmospheric neutrinos. Finally, the signal efficiency and the background rates were evaluated from MC samples.

### A. $p \rightarrow \bar{\nu}K^+$ Decay

The signal efficiencies for  $p \rightarrow \bar{\nu}K^+$  decay in KamLAND were estimated with MC simulations. We generated 10,000 event samples distributed in the complete LS volume ( $1171 \pm 25 \text{ m}^3$ ). For a free proton at rest, a two-body decay results in monochromatic kinetic energies of 339 MeV  $\bar{\nu}$  and 105 MeV  $K^+$  emitted in opposite directions. However, a bound proton decay in  $^{12}\text{C}$  will experience various nuclear effects: its Fermi-motion, the nuclear binding energy, and intra-nuclear cascades triggered by  $K^+$ -nucleon interactions. In order to model these effects, we used a nucleon decay event generator in the GENIE-based MC code (version 2.8.0) [12]. GENIE is usually used for neutrino interactions with nuclear targets, however, the code provides models of nucleon states in a nucleus and intra-nuclear hadron transport after neutrino interactions, which are essential also for nucleon decay simulations.

The distribution of momenta and binding energies of the nucleons in  $^{12}\text{C}$  is modeled by the so-called ‘‘spectral function of Benhar’’ [13], which reproduces the experimental data of electron- $^{12}\text{C}$  scattering. In the original GENIE code, the two-body decay of a nucleon was calculated based on a simple Fermi gas model ignoring the shell structure of the nucleus and nucleon-nucleon correlations, and the modification of decay nucleon mass by nuclear binding energy was absent. We implemented the mass correction,  $m'_N = m_N - E_b$  ( $E_b$ : nuclear binding energy) and the corresponding Fermi-momentum based on the spectral function providing a more realistic description of nucleon states in  $^{12}\text{C}$ .

The produced hadron from nucleon decay is simulated by the intra-nuclear cascade model in GENIE. It describes the hadronic interactions with each nucleon inside the remnant

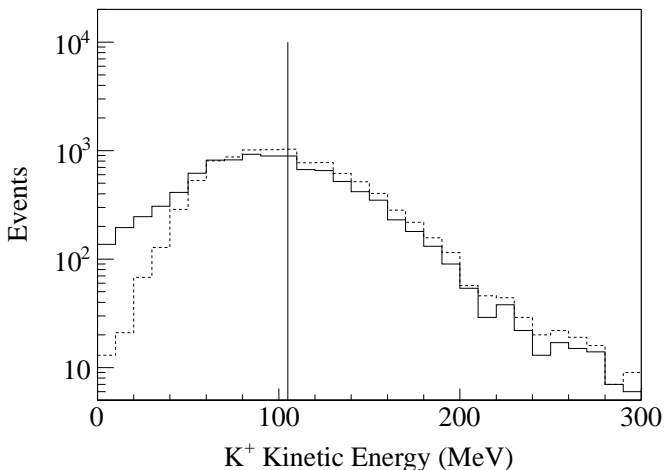


FIG. 1: The  $K^+$  kinetic energy distribution from bound proton decays in  $^{12}\text{C}$  with (solid line) and without (dashed line) the intra-nuclear cascade. The monochromatic line indicates the  $K^+$  kinetic energy for free proton decays.

nucleus before exiting. A bound proton decay of  $p \rightarrow \bar{\nu}K^+$  in  $^{12}\text{C}$  produces  $K^+$  with low momentum, below 600 MeV/c, so only elastic scattering ( $K^+p \rightarrow K^+p$  or  $K^+n \rightarrow K^+n$ ) and charge exchange ( $K^+n \rightarrow K^0p$ ) with nucleons in  $^{11}\text{B}$  can occur. In order to describe the  $K^+$  interaction with nucleons more accurately, we modified the GENIE code to implement elastic scattering and charge exchange reactions calculated based on the data-driven cross sections from partial-wave analysis [14, 15]. The  $K^+$  loss probability due to charge exchange is calculated to be only 2.1%. Figure 1 shows the resulting  $K^+$  kinetic energy distribution for bound proton decays in  $^{12}\text{C}$ . The smearing of the peak is mainly due to the Fermi-momentum. For the case of  $K^+$ -nucleon interactions, we calculated the energy loss of  $K^+$  and the energy transfer to secondaries, such as protons or neutrons, which have different scintillation response.

The initial  $K^+$  generation with MC is followed by a set of processes for particle tracking, scintillation photon emission, and photon propagation using a separate MC code based on Geant4 [16]. The detector response MC code was tuned to reproduce the data of radioactive source  $\gamma$ -rays for low energies and atmospheric neutrinos for high energies. The scintillation and optical parameters for the MC, such as Birk's constant, light output, light attenuation length, re-emission or scattering probability, are determined separately for Period-I and Period-II. The time jitter and waveform for each gain channel for the 17-inch PMTs are measured with Dye-laser calibration data. These are used to simulate the photon arrival time in the detector response MC output.

## B. Atmospheric Neutrino Background

The backgrounds from atmospheric neutrinos are estimated with MC simulations. We used the GENIE-based MC event generator assuming a atmospheric neutrino flux of Ref. [17].

The three-flavor neutrino oscillations based on the best-fit parameters given in Ref. [18] were taken into account. The detector simulation after the event generation is performed by the MC code based on Geant4 [16] as introduced above. We produced 20,000 atmospheric neutrino MC events in KamLAND which corresponds to about 100 year livetime.

The reactions are dominated by quasi-elastic scattering below 1 GeV, producing a charged-lepton in a charged-current (CC) or a recoil nucleon in a neutral current (NC). While those reactions overlap with the  $p \rightarrow \bar{\nu}K^+$  signal in the visible energy, the backgrounds can be effectively suppressed by the delayed coincidence requirement. The background rate from the mis-identification of one pulse is estimated in the following section.

Other potential background sources are kaons produced by the neutrino interactions. The GENIE code simulates kaon productions via resonances, i.e., the nucleon excitation and subsequent decay of resonances, based on the Rein-Sehgal model [19]. These reactions conserve strangeness, resulting in pair production of kaons and hyperons in the final state, such as  $\nu_\mu + n \rightarrow \mu^- + \Lambda + K^+$ . Based on the GENIE calculation, the number of events below 2 GeV with a  $K^+$  produced via a resonance is expected to be only 0.2 in the data-set. On the other hand, non-resonant kaon production, such as  $\nu_\mu + p \rightarrow \mu^- + p + K^+$ , is not considered in the GENIE code. Although experimental confirmation of such reactions is absent, these cross sections are calculable theoretically [20]. While they are comparable with the cross sections for resonant  $K^+$  production, due to the lower reaction thresholds, non-resonant kaon production can be a more important background in the  $p \rightarrow \bar{\nu}K^+$  search. Based on the cross sections in Ref. [20], the number of events below 2 GeV is expected to be only 0.14 in the data-set. Therefore, the background contributions from both resonant and non-resonant kaon pro-

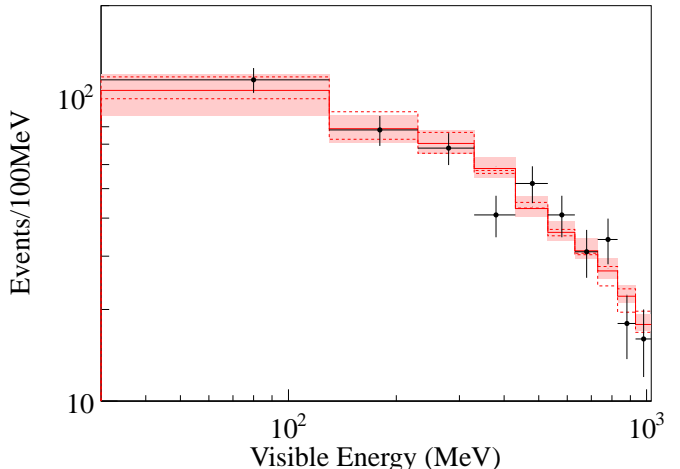


FIG. 2: Reconstructed energy spectrum of atmospheric neutrino candidates (black dots) within a 5-m-radius volume. The atmospheric neutrino MC (solid line) is normalized to the livetime of data. The neutrino interaction uncertainties evaluated by the GENIE code are indicated by the shaded region. The expectations for the linear energy scaling with  $\pm 1\sigma$  are also shown (dashed lines).

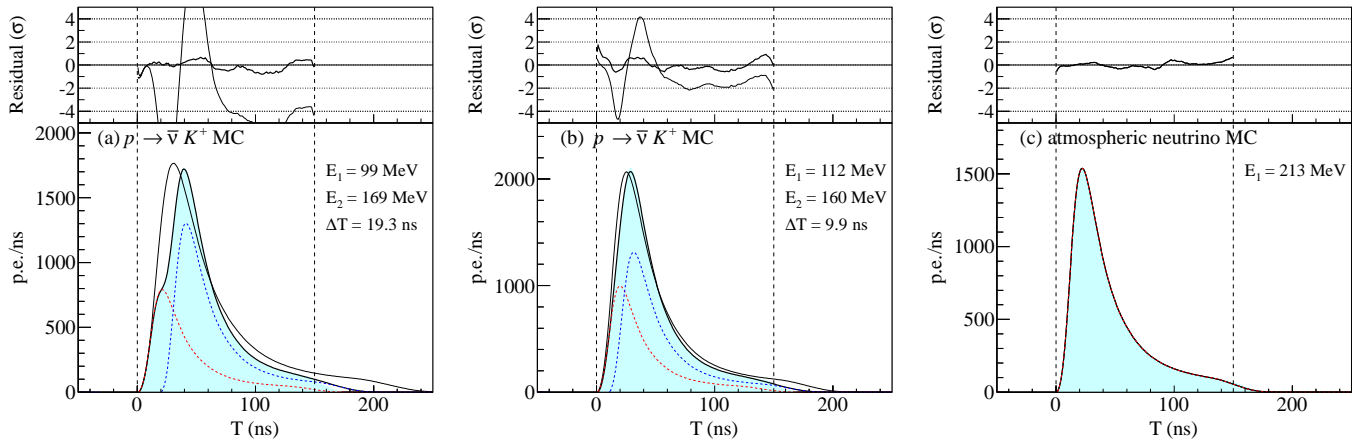


FIG. 3: Typical waveform shape (shaded) expected from: (a) and (b)  $p \rightarrow \bar{\nu} K^+$  MC example events and (c) an atmospheric neutrino MC event, together with the best-fit curves from the multi-pulse fit (solid thick line) and from the single-pulse fit (solid thin line). In the upper panel, the residuals from the best-fit are shown to identify multi-pulse events. The fitted time difference between the first pulse from  $K^+$  (red dashed line) and the second pulse from  $K^+$  decay daughters of  $\mu^+$  (blue dashed line), and their reconstructed energies are shown. The shape parameters (see text) are (a)  $\log(L_{shape}) = 0.06$  and (b)  $\log(L_{shape}) = 0.02$ .

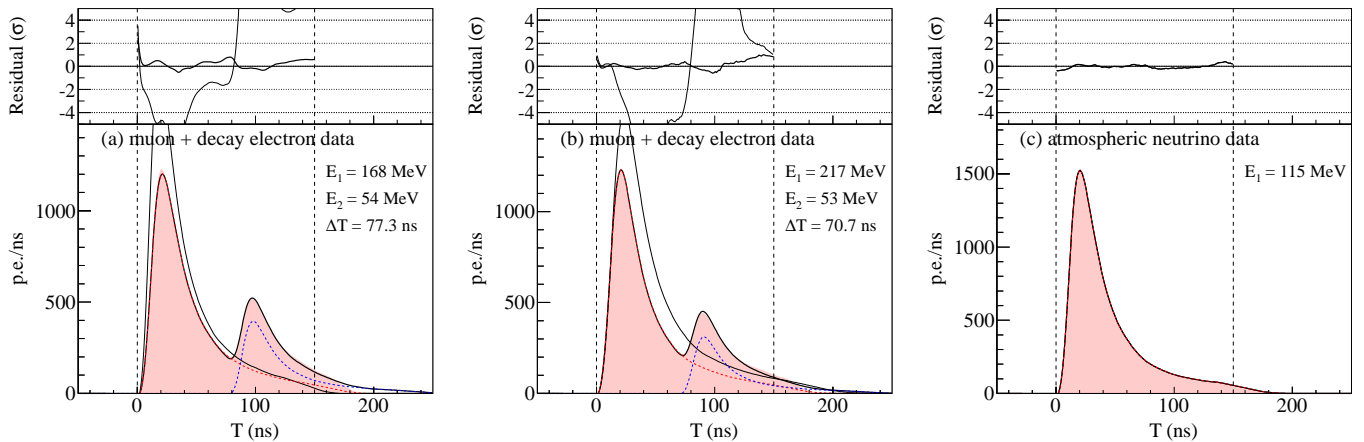


FIG. 4: Typical waveform shape (shaded) expected from: (a) and (b) muon + decay electron data and (c) atmospheric neutrino data, together with the best-fit curves from the multi-pulse fit (solid thick line) and from the single-pulse fit (solid thin line). In the upper panel, the residuals from the best-fit are shown to identify multi-pulse events. The fitted time difference between the first pulse from muons (red dashed line) and the second pulse from decay electrons (blue dashed line), and their reconstructed energies are shown.

ductions are not significant for the current  $p \rightarrow \bar{\nu} K^+$  search in KamLAND.

#### IV. ANALYSIS

In order to remove backgrounds, we apply two prior selections for proton decay events: (i) the reconstructed energy based on the PMT charge recorded within 150 ns event window is required to be more than 30 MeV and (ii) the number of OD PMT hits is less than 5. Unlike the much more frequent radioactive decays, most of the  $p \rightarrow \bar{\nu} K^+$  decays are expected to deposit a much higher energy, typically peaked at 260 MeV including short-lived decay daughter contributions, so the radioactive backgrounds can be effectively suppressed with (i). The event rate of cosmic-ray muons which pass through the

ID is about 0.3 Hz, but those muons can be rejected by the OD tagging of (ii). The inefficiency of the OD is estimated to be about 0.2%, and the remaining muons are rejected by the PMT hit-time distribution, discussed later. The events after those prior selections are dominated by atmospheric neutrinos. In addition, the small contribution of events in time-coincidence with the neutrino beam of the T2K experiment [21] are rejected. Figure 2 shows the reconstructed energy spectrum of candidate events within 5-m-radius volume after the prior selections. The observed spectrum is consistent with the expectation from the MC simulation. The uncertainty of the energy scale model, discussed in Section V, is constrained from this data.

These high energy candidates were used for the  $p \rightarrow \bar{\nu} K^+$  signal search. In order to identify the successive signals from  $K^+$  and its decay daughters in a short time, we decompose

one event into multiple pulses based on the binned- $\chi^2$  fit to the sum of the waveforms from all hit 17-inch PMTs. The waveform is a function of the photon arrival time after subtracting the time of flight (TOF) from the vertex to each PMT. The average waveform for high energy candidates is used as the reference pulse for the fit. Considering the energy and position dependence of the waveform shape, the reference pulse was prepared for each energy-position bin. The binned- $\chi^2$  for multi-pulse is defined as

$$\chi_M^2 = \sum_i \left[ f(T_i) - \frac{E_1}{E} \phi(T_i) - \frac{E_2}{E} \phi(T_i - \Delta T_{21}) - \frac{E_3}{E} \phi(T_i - \Delta T_{31}) \right]^2 / \sigma^2(T_i), \quad (1)$$

where  $f(T_i)$  is the observed waveform sum for the  $i$ -th bin (bin width is 1 ns) as a function of  $T$  ( $0 < T < 150$  ns),  $\phi(T_i)$  the reference pulse,  $E_{1,2,3}$  the energy contribution for each pulse, and  $\Delta T_{21(31)}$  the time difference between the first pulse and the second (third) pulse.  $\chi_{M=1}^2$  and  $\chi_{M=2}^2$  are defined as Eq. (1) with  $E_2 = E_3 = 0$  and  $E_3 = 0$ , respectively.  $\sigma^2(T_i)$  is calculated by

$$\sigma^2(T_i) = \left( \frac{E_1}{E} \Delta\phi(T_i) \right)^2 + \left( \frac{E_2}{E} \Delta\phi(T_i - \Delta T_{21}) \right)^2 + \left( \frac{E_3}{E} \Delta\phi(T_i - \Delta T_{31}) \right)^2, \quad (2)$$

where  $\Delta\phi(T_i)$  is the statistical fluctuation ( $1\sigma$  deviation) of the reference pulse evaluated by the MC simulation. Since atmospheric neutrino interactions can produce electromagnetic shower, the waveform shape may change. In order to account for such fluctuations, the parameter  $\alpha$  is introduced to scale the time ( $T \rightarrow \alpha T$ ) of the first pulse, is floated to fit the peak time within the uncertainty. The second pulse is mainly for  $K^+$  decay daughters of  $\mu^+$ , and the third pulse is for its decay daughter of  $e^+$ . The endpoint energy of Michel  $e^+$  from a muon decay is 52 MeV, so the allowed range of  $E_3$  is set to less than 70 MeV, taking the energy resolution into consideration.

Figure 3 (a) and (b) show the multi-pulse fit results for typical  $p \rightarrow \bar{\nu}K^+$  MC events, providing the time difference between the first pulse from  $K^+$  and the second pulse from  $K^+$  decay daughters of  $\mu^+$  ( $\Delta T$ ), and their energies ( $E_{1,2}$ ). Figure 4 (a) and (b) show the multi-pulse fit result for typical multi-pulse events from muon + decay electron data, providing the time difference between the first pulse from muon and the second pulse from muon decay daughters of electron ( $\Delta T$ ), and their energies ( $E_{1,2}$ ).

We require the following criteria to select the  $p \rightarrow \bar{\nu}K^+$  signal:

- (1) The distance from the center of the detector to the reconstructed vertex ( $R$ ) is less than 6.5 m, which corresponds to the full LS volume.
- (2) The PMT hit time distribution is selected to be point-like or moderately track-like to reject cosmic-ray muons

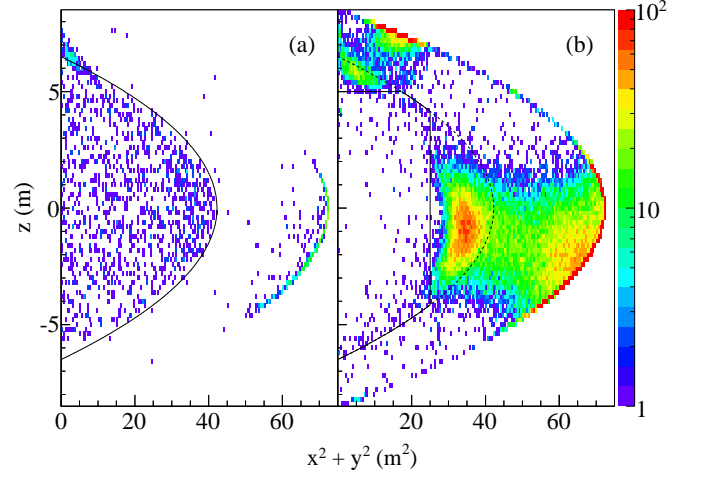


FIG. 5: Vertex distribution of atmospheric neutrino candidates in the energy range of 30–1000 MeV for (a) point-like events ( $\chi_T^2 < 1.2$ ) and (b) track-like events ( $1.2 \leq \chi_T^2 < 5.0$ ).

which have long tracks in the ID. Specifically, the time-based  $vertex\text{-}\chi^2$  ( $\chi_T^2$ ), which compares the observed PMT hit time distribution as a function of distance to the event to the expected distributions, is required to be less than 1.2 (point-like) for all volume or between 1.2 and 5.0 (track-like) for  $z < 5.0$  m and  $x^2 + y^2 < 25$  m<sup>2</sup>.

- (3) The time difference between the first pulse and the second pulse ( $\Delta T$ ) is between 7 and 100 ns, considering the  $K^+$  lifetime of 12.4 ns.
- (4) The reconstructed energy of the first pulse ( $E_1$ ) is between 30 and 300 MeV, the second pulse ( $E_2$ ) between 70 and 600 MeV, as constrained by the decay kinematics.
- (5) The waveform shape is multi-pulse-like to reject single-pulse events. We use a waveform shape parameter defined as  $\log(L_{shape}) \equiv \log(\Delta\chi^2) - \lambda$ , where  $\Delta\chi^2 = \chi_{M=1}^2 - \chi_{M=2,3}^2$  and  $\lambda$  the mean of the  $\log(\Delta\chi^2)$  distributions evaluated with the  $p \rightarrow \bar{\nu}K^+$  MC as a function of  $\Delta T$ .  $\log(\Delta\chi^2)$  is required to be more than  $-0.5$ .

The backgrounds from OD untagged cosmic-ray muons concentrate in the top and equator regions of the detector because the water Cherenkov active volume outside these regions are relatively thin. Figure 5 shows the vertex distributions of atmospheric neutrino candidates in the energy range of 30–1000 MeV. Only for track-like events ( $1.2 \leq \chi_T^2 < 5.0$ ), we apply a tighter volume cut ( $z < 5.0$  m and  $x^2 + y^2 < 25$  m<sup>2</sup>) to reject OD untagged muons concentrated in the top and equator regions.

Figure 6 shows the distributions of reconstructed energies of the two pulses ( $E_1, E_2$ ) for data, atmospheric neutrino MC events, and  $p \rightarrow \bar{\nu}K^+$  MC events, after all cuts except (4). The main background sources are mis-identified single-pulse events due to the limited multi-pulse separation power in the fit. For  $p \rightarrow \bar{\nu}K^+$ , there are two bands corresponding to stopped  $K^+$  decays,  $K^+ \rightarrow \mu^+\nu_\mu$  with a branching ratio of 63.55% (the kinetic energy of the  $\mu^+$  is 152 MeV) and

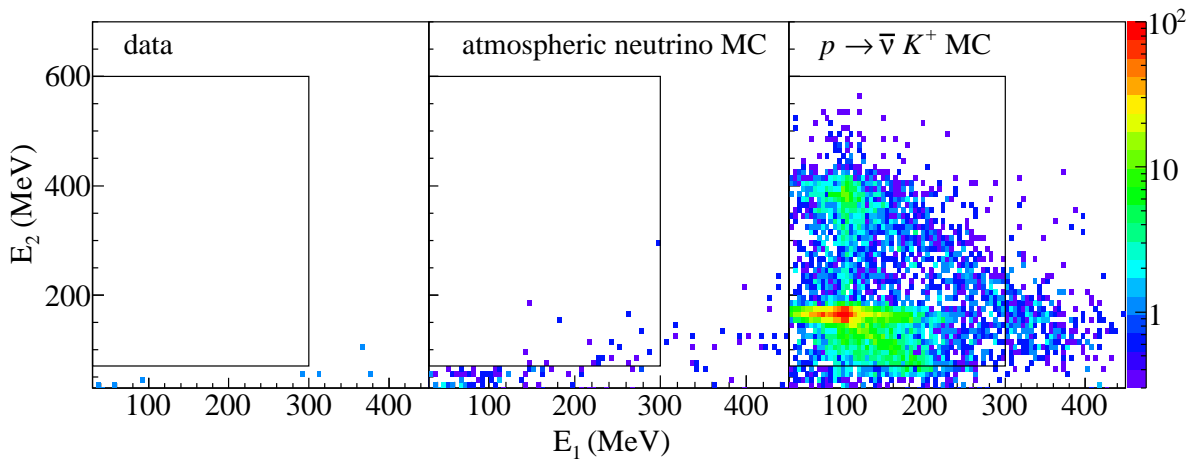


FIG. 6: Distribution of reconstructed energies of the two pulses  $E_1$  and  $E_2$  for data (left), atmospheric neutrino MC events (middle), and  $p \rightarrow \bar{\nu}K^+$  MC events (right). The box shows the selection cuts for  $E_1$  and  $E_2$ .

TABLE I: Main decay modes of  $K^+$  in descending order of branching ratio [18]. The prompt  $K^+$  signal is followed by delayed signals from  $K^+$  decay daughters. Their kinetic energies which contribute to instantaneous scintillation are summed up.

Decay mode	branching ratio (%)	kinetic energy sum (MeV)
$K^+ \rightarrow \mu^+ \nu_\mu$	$63.55 \pm 0.11$	152
$K^+ \rightarrow \pi^+ \pi^0$	$20.66 \pm 0.08$	354
$K^+ \rightarrow \pi^+ \pi^+ \pi^-$	$5.59 \pm 0.04$	75
$K^+ \rightarrow \pi^0 e^+ \nu_e$	$5.07 \pm 0.04$	265–493
$K^+ \rightarrow \pi^0 \mu^+ \nu_\mu$	$3.353 \pm 0.034$	200–388
$K^+ \rightarrow \pi^+ \pi^0 \pi^0$	$1.761 \pm 0.022$	354

$K^+ \rightarrow \pi^+ \pi^0$  with a branching ratio of 20.66% (the sum of kinetic energies of the  $\pi^+$  and the  $\pi^0$ -decay-induced gammas is 354 MeV). The difference between the visible energies and the real energies is explained by non-linear scintillation response introduced by quenching depending on the ionization density of charged particles. The spread in  $E_2$  is due to the multi-pulse separation uncertainty for the case of the smaller time difference between the first and second pulses or contributions from other  $K^+$  decay modes. Figure 7 shows the distribution of the shape parameter for data, atmospheric neutrino MC, and  $p \rightarrow \bar{\nu}K^+$  MC, after all cuts except (5). The atmospheric neutrino backgrounds from mis-identification of single-pulse events tends to have lower  $L_{shape}$  as expected. The expected number of atmospheric neutrino background events is  $0.9 \pm 0.2$  in total. No data remain after all cuts.

## V. EFFICIENCIES AND SYSTEMATIC UNCERTAINTIES

Table II shows the detection efficiencies estimated from  $p \rightarrow \bar{\nu}K^+$  MC at each event reduction step for the five selection criteria. The MC statistical uncertainty is less than 0.5%. The large inefficiencies, caused by the selection criteria of (3)

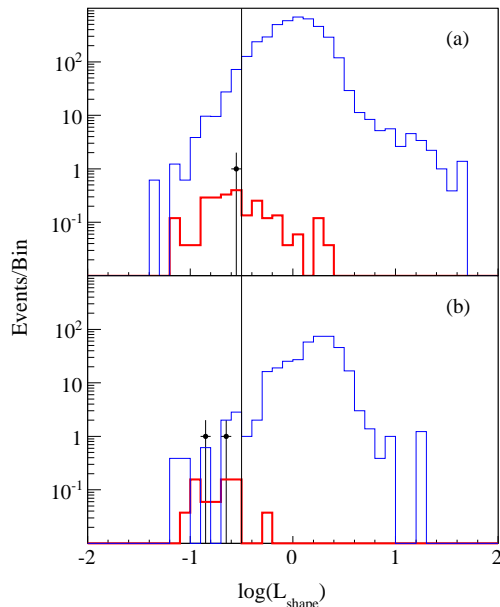


FIG. 7: Shape parameter ( $L_{shape}$ ) distributions of data (black dot), atmospheric neutrino MC (thick red line), and  $p \rightarrow \bar{\nu}K^+$  MC (thin blue line) for (a) point-like events ( $\chi^2_T < 1.2$ ) and (b) track-like events ( $1.2 \leq \chi^2_T < 5.0$ ). The contribution of the atmospheric neutrino background is normalized to the livetime of data.

and (4), are highly dependent on the multi-pulse separation power in the fit. The decrease of the detection efficiencies for the case of  $K^+$  decay within a short time is illustrated in Figure 8. The total efficiencies for  $p \rightarrow \bar{\nu}K^+$  in the LS are estimated to be  $0.444 \pm 0.053$  for Period-I and  $0.432 \pm 0.050$  for Period-II, considering the systematic uncertainties on the detection efficiency listed in Table III.

The number of protons is calculated based on the total LS volume ( $1171 \pm 25 \text{ m}^3$ ) measured by flow meters during detector filling, the LS density ( $0.780 \text{ g/cm}^3$ ), and the hydrogen-

TABLE II: Detection efficiencies estimated from  $p \rightarrow \bar{\nu}K^+$  MC at each event reduction step for the five selection criteria.

	Period-I	Period-II
(1) vertex cut ( $x, y, z$ )	0.979	0.978
(2) point-like cut ( $\chi_T^2$ )	0.935	0.932
(3) time cut ( $\Delta T$ )	0.658	0.624
(4) energy cut ( $E_1, E_2$ )	0.454	0.447
(5) shape cut ( $L_{\text{shape}}$ )	0.444	0.432

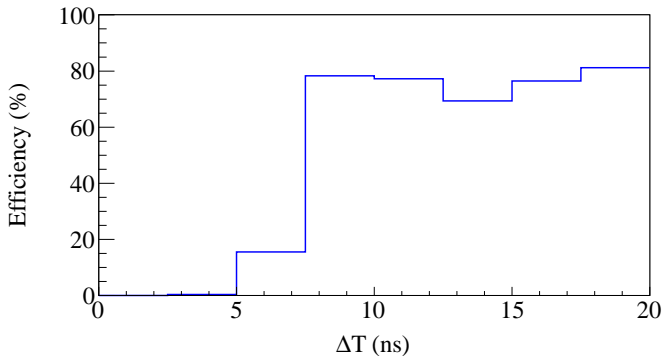


FIG. 8: Detection efficiency as a function of  $\Delta T$  estimated from  $p \rightarrow \bar{\nu}K^+$  MC in Period-I. The decrease for  $\Delta T < 7$  ns, due to poor resolution of the multi-pulse fit, is the primary source of inefficiency for the  $p \rightarrow \bar{\nu}K^+$  search.

to-carbon ratio (1.97) verified by elemental analysis. The nitrogen-to-carbon and oxygen-to-carbon ratios are negligibly small ( $< 6 \times 10^{-4}$ ). The 913 ton of LS mass contains  $7.74 \times 10^{31}$  free protons in hydrogen and  $2.33 \times 10^{32}$  bound protons in carbon, thus  $3.11 \times 10^{32}$  protons in total. The uncertainty on the number of protons is 2.1% determined from the LS volume measurement.

The detection efficiency calculation from  $p \rightarrow \bar{\nu}K^+$  MC has associated systematic uncertainties. The MC code considers  $K^+$ -nucleon interactions in  $^{12}\text{C}$ , which cause the  $K^+$  loss with a probability of 2.1% assuming the nuclear model given in Section III A. We conservatively include the size of this correction as an additional systematic uncertainty. The detector energy-scale in the low energy data is well calibrated by the radioactive source  $\gamma$ -rays, but we need to confirm that this calibration is still appropriate to extrapolate into the high energy data up to 1 GeV. So we confirmed the energy scale uncertainty from the fit to the spectral shape of atmospheric neutrino candidates below 1 GeV. We floated the linear energy scale, the normalization factors, and the two systematic parameters provided in the GENIE code: axial mass for charged-current quasi-elastic and axial mass for neutral-current elastic, which are inputs for the calculation of the nucleon form factor in nucleus and constrained within the uncertainties. The energy scale factor is fitted to  $0.95_{-0.17}^{+0.11}$  with  $\pm 1\sigma$  error as indicated in Figure 2, which corresponds to a 3.6%/1.9% uncertainty in the detection efficiency for Period-I-II.

The primary source of systematic uncertainty is a possible waveform deformation due to uncertainties in the scintillation

TABLE III: Estimated systematic uncertainties of the lifetime calculation for  $p \rightarrow \bar{\nu}K^+$ . The dominant uncertainty comes from the waveform modeling (11.1%) for the  $K^+$  signal in the detection efficiency calculation.

Source	Period-I	Period-II
Number of protons	2.1%	2.1%
Detection efficiency		
Nuclear model	2.1%	2.1%
Energy scale	3.6%	1.9%
Waveform model	11.1%	11.1%
Total systematic uncertainty	12.0%	11.6%

process. The scintillation time profile is determined from the ionization density of charged particles interacting in the LS, thus the waveform shape depends on the type of particle interacting and its energy. As there are no waveform calibration samples for  $K^+$  scintillation, we computed the efficiencies from  $p \rightarrow \bar{\nu}K^+$  MC for two extreme cases; the scintillation time profile is constructed from the low energy data for a  $\gamma$ -ray source, and for a neutron source. The ionization density of  $K^+$  from proton decays is expected to be the intermediate region between these two. We found a detection efficiency difference of 11.1% and assign it as a systematic uncertainty. The total systematic uncertainty on the lifetime calculation for  $p \rightarrow \bar{\nu}K^+$  is 12.0%/11.6% for Period-I-II, from adding the uncertainty sources summarized in Table III in quadrature.

## VI. RESULTS

We find no event excess over background predictions in the  $p \rightarrow \bar{\nu}K^+$  search. The lower limit on the partial proton lifetime is obtained from:

$$\tau/B(p \rightarrow \bar{\nu}K^+) > \frac{N_p}{n_{\text{limit}}} \sum_{i=1,2} T_i \epsilon_i \quad (3)$$

where  $N_p$  is the number of protons in the whole LS volume,  $T_i$  is the detector lifetime,  $\epsilon_i$  is the detection efficiency for Period-I ( $i = 1$ ) and Period-II ( $i = 2$ ), given in Table II, and  $n_{\text{limit}}$  is the estimated upper limit on the number of events for the  $p \rightarrow \bar{\nu}K^+$  signal. Considering the large uncertainty of the background estimate, we conservatively calculate  $n_{\text{limit}}$  assuming zero background. Using the Feldman-Cousins procedure [22] which accounts for the errors on nuisance parameters listed in Table III,  $n_{\text{limit}} = 2.44$  events at 90% C.L. and the corresponding lifetime limit is  $\tau/B(p \rightarrow \bar{\nu}K^+) > 5.4 \times 10^{32}$  years.

## VII. DISCUSSION

We demonstrated a sensitive search for the proton decay mode  $p \rightarrow \bar{\nu}K^+$  with the coincidence method. While the search sensitivity in KamLAND is about an order of magnitude smaller than a previous search in Super-Kamiokande due

to the more limited exposure, we confirm the conclusion that the SUSY SU(5) GUT with minimal assumption predicting the partial lifetime of  $\tau/B(p \rightarrow \bar{\nu}K^+) \lesssim 10^{30}$  years is excluded. Extended SUSY-GUT models giving a partial lifetime of  $\tau/B(p \rightarrow \bar{\nu}K^+) \gtrsim 10^{33}$  years are still beyond our search range. However, our search sensitivity has not been limited by backgrounds yet due to the effective background suppression by the coincidence method. It indicates that future increases in statistics is possible with LS detectors.

Several future tens-of-kton LS detectors at different underground sites are proposed to investigate various physics topics. The LENA experiment was planned to perform a sensitive search for  $p \rightarrow \bar{\nu}K^+$ , and the potential of a LS detector with a fiducial mass of 50 kton was investigated [23]. Assuming a projected detection efficiency of 65%, the search sensitivity is expected to reach  $\tau/B(p \rightarrow \bar{\nu}K^+) \sim 4 \times 10^{34}$  years at 90% C.L. within ten years, so the extended SUSY-GUT models can be tested. The higher efficiency in LENA is mainly due to the clear discrimination of atmospheric neutrino backgrounds based on pulse risetime measurements. We find that the risetime is not stable from the atmospheric neutrino MC studies. In the case of LENA, kaon productions induced by the atmospheric neutrino interactions, discussed in Section III B, are non-negligible. However, if the background discrimination by counting the number of decay electrons suggested in Ref. [23] works, a background-free search will still be possible.

## VIII. CONCLUSION

We have presented a search for the proton decay mode  $p \rightarrow \bar{\nu}K^+$  with the KamLAND liquid scintillator detector.

We found no evidence of proton decays, and obtained a lower limit on the partial proton lifetime,  $\tau/B(p \rightarrow \bar{\nu}K^+) > 5.4 \times 10^{32}$  years at 90% C.L. Due to KamLAND's smaller detector size, the limit is less stringent than the latest Super-Kamiokande result,  $\tau/B(p \rightarrow \bar{\nu}K^+) > 5.9 \times 10^{33}$  years at 90% C.L. However, the detection efficiency in KamLAND is about two times better relative to Super-Kamiokande for background-free searches, so future searches with large liquid scintillator detectors are expected to be competitive with the current limit. Such improved searches will test SUSY-GUT models more stringently.

## ACKNOWLEDGMENTS

We thank T. Kitagaki for advice and guidance. The KamLAND experiment is supported by the Grant-in-Aid for Specially Promoted Research under grant 16002002 and 21000001 of the Japanese Ministry of Education, Culture, Sports, Science and Technology; the World Premier International Research Center Initiative (WPI Initiative), MEXT, Japan; Stichting FOM in the Netherlands; and under the US Department of Energy (DOE) Grant No. DE-AC02-05CH11231 and DE-FG02-01ER41166, as well as other DOE grants to individual institutions. The Kamioka Mining and Smelting Company has provided service for activities in the mine. We thank the support of NII for SINET4.

- 
- [1] J. Wess and B. Zumino, Nucl. Phys. B **70**, 39 (1974).
  - [2] W. Marciano and G. Senjanović, Phys. Rev. D **25**, 3092 (1982).
  - [3] H. Murayama and A. Pierce, Phys. Rev. D **65**, 055009 (2002).
  - [4] K. S. Hirata *et al.*, Phys. Lett. B **220**, 308 (1989).
  - [5] C. McGrew *et al.*, Phys. Rev. D **59**, 052004 (1999).
  - [6] H. Nishino *et al.*, (Super-Kamiokande Collaboration), Phys. Rev. Lett. **102**, 141801 (2009).
  - [7] A. Gando *et al.*, (KamLAND Collaboration), Phys. Rev. D **88**, 033001 (2013).
  - [8] Y. Hayato *et al.*, (Super-Kamiokande Collaboration), Phys. Rev. Lett. **83**, 1529 (1999).
  - [9] K. Kobayashi *et al.*, (Super-Kamiokande Collaboration), Phys. Rev. D **72**, 052007 (2005).
  - [10] K. Abe *et al.*, (Super-Kamiokande Collaboration), Phys. Rev. D **90**, 072005 (2014).
  - [11] A. Gando *et al.*, (KamLAND-Zen Collaboration), Phys. Rev. Lett. **110**, 062502 (2013).
  - [12] C. Andreopoulos *et al.*, Nucl. Instrum. and Meth. A **614**, 87 (2010).
  - [13] O. Benhar, N. Farina, H. Nakamura, M. Sakuda, and R. Seki, Phys. Rev. D **72**, 053005 (2005).
  - [14] M. Hoffmann, J. W. Durso, K. Holinde, B. C. Pearce, and J. Speth, Nucl. Phys. A **593**, 341 (1995).
  - [15] V. E. Tarasov, V. V. Khabarov, A. E. Kudryavtsev, and V. M. Weinberg, Phys. of Atom. Nucl. **71**, 1410 (2008).
  - [16] J. Allison *et al.*, IEEE Trans. Nucl. Sci. **53**, 270 (2006).
  - [17] M. Honda, T. Kajita, K. Kasahara, and S. Midorikawa, Phys. Rev. D **83**, 123001 (2011).
  - [18] K. A. Olive *et al.* (Particle Data Group), Chin. Phys. C **38** (2014).
  - [19] D. Rein and L. M. Sehgal, Ann. of Phys. **133**, 79 (1981).
  - [20] M. Rafi Alam, I. Ruiz Simo, M. Sajjad Athar, and M. J. Vicente Vacas, Phys. Rev. D **82**, 033001 (2010).
  - [21] K. Abe *et al.*, (T2K Collaboration), Phys. Rev. Lett. **112**, 061802 (2014).
  - [22] G. J. Feldman and R. D. Cousins, Phys. Rev. D **57**, 3873 (1998).
  - [23] T. M. Undagoitia *et al.*, Phys. Rev. D **72**, 075014 (2005).